

## THE DOMINANCE OF METAL-RICH STREAMS IN STELLAR HALOS: A COMPARISON BETWEEN SUBSTRUCTURE IN M31 AND $\Lambda$ CDM MODELS

KAROLINE M. GILBERT<sup>1</sup>, ANDREEA S. FONT<sup>2</sup>, KATHRYN V. JOHNSTON<sup>3</sup>, PURAGRA GUHATHAKURTA<sup>4</sup>

*Accepted for publication in ApJ*

### ABSTRACT

Extensive photometric and spectroscopic surveys of the Andromeda galaxy (M31) have discovered tidal debris features throughout M31's stellar halo. We present stellar kinematics and metallicities in fields with identified substructure from our on-going SPLASH survey of M31 red giant branch stars with the DEIMOS spectrograph on the Keck II 10-m telescope. Radial velocity criteria are used to isolate members of the kinematically-cold substructures. The substructures are shown to be metal-rich relative to the rest of the dynamically hot stellar population in the fields in which they are found. We calculate the mean metallicity and average surface brightness of the various kinematical components in each field, and show that, on average, higher surface brightness features tend to be more metal-rich than lower surface brightness features. Simulations of stellar halo formation via accretion in a cosmological context are used to illustrate that the observed trend can be explained as a natural consequence of the observed dwarf galaxy mass-metallicity relation. A significant spread in metallicity at a given surface brightness is seen in the data; we show that this is due to time effects, namely the variation in the time since accretion of the tidal streams' progenitor onto the host halo. We show that in this theoretical framework a relationship between the alpha-enhancement and surface brightness of tidal streams is expected, which arises from the varying times of accretion of the progenitor satellites onto the host halo. Thus, measurements of the alpha-enrichment, metallicity, and surface brightness of tidal debris can be used to reconstruct the luminosity and time of accretion onto the host halo of the progenitors of tidal streams.

*Subject headings:* galaxies: substructure — galaxies: halo — galaxies: individual (M31)

### 1. INTRODUCTION

In a hierarchical universe, a large galaxy will undergo many mergers during its lifetime. The amount and properties of accreted material observed in present-day galaxies can be used to test hierarchical formation scenarios. Stellar halos provide an ideal environment for investigating the detailed merger history of an individual galaxy. The sparse stellar populations of a galaxy's halo combined with long dynamical times make it possible for tidal debris features to remain identifiable in phase-space for billions of years. In contrast, it is difficult to separate material formed in situ from accreted material in a galaxy's relatively dense disk and bulge.

Recent sophisticated numerical and semianalytic simulations of stellar halo formation have made great strides in characterizing the properties of stellar halos that are built up through the tidal stripping of accreted satellites (e.g., Johnston et al. 1996; Johnston 1998; Helmi & White 1999; Helmi & de Zeeuw 2000; Bullock et al. 2001). Bullock & Johnston (2005) (hereafter BJ05) used a combination of  $N$ -body and semi-analytic techniques to simulate the formation via accretion of 11 MW-analog stellar halos in a cosmological context. These high resolution simulations allow detailed analysis of the expected physical properties of stellar halos composed primarily of

tidal debris and their associated satellite systems (Font et al. 2006a,b, 2008; Johnston et al. 2008).

The stellar halos of the Milky Way (MW) and Andromeda (M31) galaxies both show ample evidence of recent and on-going accretion events. Among the most prominent of these substructures are the Sagittarius stream (Ibata et al. 1994; Majewski et al. 2003; Newberg et al. 2003) and the Monoceros stream (Yanny et al. 2003; Rocha-Pinto et al. 2003) in the MW, and the giant southern stream (GSS; Ibata et al. 2001) in M31, which likely pollutes much of M31's spheroid interior to  $\sim 20$ – $30$  kpc (Fardal et al. 2007; Gilbert et al. 2007; Richardson et al. 2008).

In addition to these prominent stellar streams, recent large observational surveys are increasing the number of known tidal debris features by pushing to lower surface brightness limits. Analysis of the Sloan Digital Sky Survey has revealed many faint tidal debris features in the MW's stellar halo (e.g., Grillmair 2006; Grillmair & Dionatos 2006; Belokurov et al. 2006, 2007), while large-scale photometric studies of M31 are revealing similarly large numbers of tidal debris features in M31's stellar halo (Ibata et al. 2001, 2007). Spectroscopic surveys of red giant branch (RGB) stars in M31 (Irwin et al. 2005; Kalirai et al. 2006a; Gilbert et al. 2006) are enabling the discovery of tidal debris features through the kinematics of M31's stellar populations (e.g., Ibata et al. 2005; Kalirai et al. 2006b; Gilbert et al. 2007; Chapman et al. 2008; Gilbert et al. 2009).

A classic signature of substructure is an abnormally high surface brightness relative to the value expected from the observed surface brightness profile of the stellar halo. Due to the long dynamical times in the sparse outer regions of galaxy halos, tidal debris from relatively recent mergers (within the last several Gyr) will not have

Electronic address: kgilbert@astro.washington.edu

<sup>1</sup> Department of Astronomy, University of Washington, Box 351580, Seattle, WA, 98195-1580.

<sup>2</sup> Institute for Computational Cosmology, University of Durham, Science Laboratories, South Road, Durham DH1 3LE, UK

<sup>3</sup> Department of Astronomy, Columbia University, Pupin Physics Laboratory, 550 West 120th Street, New York, New York 10027

<sup>4</sup> UCO/Lick Observatory, Department of Astronomy & Astrophysics, University of California Santa Cruz, 1156 High Street, Santa Cruz, California 95064.

had time to become spatially well-mixed. The kinematical distribution of a well-mixed stellar halo population is expected to be broad (dynamically hot) out to large distances from the center of the galaxy. In the MW and M31, the measured line-of-sight velocity dispersion is  $\sigma_v \sim 120$  to  $150 \text{ km s}^{-1}$  near the galaxy’s center (Battaglia et al. 2005; Chapman et al. 2006; Gilbert et al. 2007) and decreases to  $\sigma_v \sim 100 \text{ km s}^{-1}$  at  $R \sim 60 \text{ kpc}$  (Battaglia et al. 2005; Chapman et al. 2006). In contrast, tidal debris from a single accretion event should be dynamically cold, since the local velocity dispersion of the debris should decrease as it mixes along the progenitor satellite’s orbit: as the stars spread apart, decreasing their spatial density, their density in velocity-space must increase in order to conserve their phase-space density and satisfy Liouville’s theorem (Helmi & White 1999). Hence, kinematical substructure in a survey is another signature of hierarchical structure formation. A difference in chemical abundance between stars in the kinematically hot and cold populations or between two closely spaced fields is also evidence of substructure, as the progenitors of recent accretion events are likely to be chemically distinct from the ensemble of satellites that were accreted at early times.

We have utilized the kinematical and chemical signatures of substructure to identify multiple, kinematically cold tidal debris features (Guhathakurta et al. 2006; Kalirai et al. 2006b; Gilbert et al. 2007, 2009) during the course of the Spectroscopic and Photometric Landscape of Andromeda’s Stellar Halo (SPLASH) Survey which includes extensive Keck/DEIMOS<sup>5</sup> spectroscopic survey of M31’s stellar halo (e.g., Guhathakurta et al. 2005; Kalirai et al. 2006a; Gilbert et al. 2006, 2007). Kinematical signatures of substructure enable the detection of faint and diffuse features which are not easily identified in star-count maps. For example, a shelf feature (Gilbert et al. 2007) along M31’s southeast minor axis ( $R_{\text{proj}} \sim 12\text{--}18 \text{ kpc}$ ) went unnoticed on star count maps (in fact, the region was specifically targeted for deep HST photometry based on its apparent smoothness; Brown et al. 2003). The observed distribution of stars in line-of-sight velocity vs. position space and its striking similarity to model predictions led to the discovery of the SE shelf.

We can use the kinematically cold tidal debris features found in our survey to study general trends of tidal debris in stellar halos. The recent advances in simulations of stellar halo formation have made it possible to undertake detailed comparisons of the properties of observed and simulated substructure (Bell et al. 2008; Font et al. 2008). In this contribution, we present a relationship between the surface brightness and metallicity of tidal debris features observed in our M31 data set, and provide a physical interpretation of the observed trend through comparisons of the observations with simulated stellar streams in the BJ05 simulations.

The paper is organized as follows. In §2 we briefly discuss the observations and reduction techniques and present the fields in our M31 survey in which substructure

has been identified. We present the kinematical and chemical abundance distributions of the stars in these fields as well as the surface brightness and average metallicity of the observed kinematical substructures. The methods used in the BJ05 simulations are outlined in §3, and the trends of surface brightness with chemical abundance of stellar streams in the simulated BJ05 stellar halos are presented. We compare the observations with the simulations and discuss the resulting physical implications in §4. Finally, we summarize our results in §5.

## 2. DATA

### 2.1. Photometric and Spectroscopic Observations

The photometric and spectroscopic observations and data reductions employed in our SPLASH M31 survey have been discussed in detail in previous papers (Guhathakurta et al. 2006; Kalirai et al. 2006b; Gilbert et al. 2006, 2007) and will be only briefly outlined here. The observations are organized into “fields” in M31’s stellar halo based on the spatial proximity of the spectroscopic slitmasks (Table 1). A single photometric pointing is large enough to support multiple, non-overlapping DEIMOS slitmask observations; the spectra from slitmasks based on a single photometric pointing are in general analyzed together and considered a field. The exception to this are fields f207 and H13s, which are from a single photometric pointing but are treated as separate fields due to the fact that they are located at different positions along M31’s GSS; the debris from the GSS is centered at a different mean velocity in each of these fields.

Photometry and astrometry for the SE shelf, f207, and H13s fields were derived from images in the  $g'$  and  $i'$  bands taken with the MegaCam instrument on the 3.6-m Canada-France-Hawaii Telescope (CFHT).<sup>6</sup> The SExtractor program was used for object detection, photometry, and morphological classification (Bertin & Arnouts 1996) and observations of Landolt photometric standard stars were used to transform from instrumental  $g'$  and  $i'$  magnitudes to Johnson-Cousins  $V$  and  $I$  magnitudes (Kalirai et al. 2006b).

Photometry and astrometry for the a3, a13, and m4 fields were derived by Ostheimer (2003) from images in the Washington  $M$  and  $T_2$  bands and the intermediate-width DDO51 band taken with the Mosaic camera on the 4-m Kitt Peak National Observatory (KPNO) telescope.<sup>7</sup> The DDO51 filter includes the surface-gravity sensitive  $\text{Mg}b$  and  $\text{MgH}$  stellar absorption features. The combination of these three filters allows photometric selection of stars that are likely to be M31 red giant branch (RGB) stars rather than MW dwarf stars along the line-of-sight to M31 (Majewski et al. 2005). The photometric transformation relations in Majewski et al. (2000) were used to convert the  $M$  and  $T_2$  magnitudes to Johnson-Cousins

<sup>5</sup> Data presented herein were obtained at the W. M. Keck Observatory, which is operated as a scientific partnership among the California Institute of Technology, the University of California and the National Aeronautics and Space Administration. The Observatory was made possible by the generous financial support of the W. M. Keck Foundation.

<sup>6</sup> MegaPrime/MegaCam is a joint project of CFHT and CEA/DAPNIA, at the Canada-France-Hawaii Telescope which is operated by the National Research Council of Canada, the Institut National des Science de l’Univers of the Centre National de la Recherche Scientifique of France, and the University of Hawaii.

<sup>7</sup> Kitt Peak National Observatory of the National Optical Astronomy Observatory is operated by the Association of Universities for Research in Astronomy, Inc., under cooperative agreement with the National Science Foundation

TABLE 1  
M31 SPECTROSCOPIC FIELDS WITH IDENTIFIED SUBSTRUCTURE.

Field	# Spectroscopic Masks	Projected Radius (kpc)	# Stars <sup>a</sup>	# of M31 Stars <sup>b</sup>	Reference
SE shelf	4	12–18	510	428	Gilbert et al. (2007)
f207	1	16–19	57	49	Gilbert et al. (2009)
H13s	2	20–23	212	178	Kalirai et al. (2006b), Gilbert et al. (2009)
a3	3	31–34	88	69	Guhathakurta et al. (2006), Gilbert et al. (2009)
a13	4	55–63	109	44	Gilbert et al. (2009)
m4	5	53–60	154	53	Gilbert et al. (2009)

<sup>a</sup> The total number of unique stellar spectra for which we recovered velocities.

<sup>b</sup> The number of M31 RGB stars is defined as the number of stars that are identified as secure and marginal M31 RGB stars by the Gilbert et al. (2006) diagnostic method.

$V$  and  $I$  magnitudes.

Objects were selected for spectroscopy based on their derived  $I$  magnitudes and morphological properties. In the outer fields (a3, a13, and m4), objects were further prioritized by their probability of being an M31 RGB star based on the  $M$ ,  $T_2$ , and DDO51 photometry; this is vital for increasing the spectroscopic efficiency of our survey in the sparse outer regions of M31’s stellar halo. Spectroscopic slitmasks were observed with the DEIMOS instrument on the Keck II telescope for 1 hr each, using the 1200 line  $\text{mm}^{-1}$  grating (which has a dispersion of  $0.33 \text{ \AA pixel}^{-1}$ ) centered at  $7800 \text{ \AA}$ . This led to an average spectral coverage of  $6450\text{--}9150 \text{ \AA}$ .

Modified versions of the `spec2d` and `spec1d` software<sup>8</sup> developed by the DEEP2 team at the University of California, Berkeley were used to reduce and analyze the spectroscopic data (see Simon & Geha 2007; Gilbert et al. 2007). Reduced one-dimensional spectra are cross-correlated with a library of template stellar spectra to determine the redshift of the object. Each spectrum is visually inspected and assigned a quality code based on the number and quality of the absorption lines. A spectrum must have at least two identifiable spectral features to be considered to have a secure redshift measurement (Guhathakurta et al. 2006; Gilbert et al. 2007). A heliocentric correction and a correction for possible miscentering of the star within the slit (based on the position of the telluric A-band relative to atmospheric emission lines in the observed spectrum) is applied to the measured velocities (Simon & Geha 2007; Sohn et al. 2007). The median velocity error is  $\sim 6 \text{ km s}^{-1}$ , based on error estimates from the cross-correlation routine and repeat measurements of individual stars.

## 2.2. Selection of M31 RGB Stars

The line-of-sight velocity distributions of foreground MW dwarf stars and M31 RGB halo stars overlap, making it nontrivial to identify individual stars as M31 red giants or MW dwarfs. We use the diagnostic method described in Gilbert et al. (2006) to isolate M31 RGB stars from foreground MW dwarf stars in our spectroscopic sample. Empirical probability distribution functions in five photometric and spectroscopic diagnostics

are used to determine the likelihood an individual star is an M31 red giant. These diagnostics include (1) line-of-sight velocity, (2) photometry in the  $M$ ,  $T_2$ , and DDO51 bands (when available), (3) the EW of the Na I doublet at  $8190 \text{ \AA}$  versus the  $(V - I)_0$  color of the star, (4) position of the star in an  $[I_0, (V - I)_0]$  color magnitude diagram, and (5) photometric versus spectroscopic metallicity estimates. The M31 RGB sample used in this analysis includes all stars that are more probable to be M31 red giants than MW dwarfs.

## 2.3. Metallicity Estimates

Metallicity estimates ( $[\text{Fe}/\text{H}]$ ) are derived by comparing a star’s position in the  $[I_0, (V - I)_0]$  color magnitude diagram with theoretical isochrones adjusted to the distance of M31 (783 kpc; Stanek & Garnavich 1998; Holland 1998). Interpolation within the grid of 12 Gyr,  $[\alpha/\text{Fe}]=0$ , VandenBerg et al. (2006) isochrones yields an  $[\text{Fe}/\text{H}]$  measurement for each M31 RGB star (Kalirai et al. 2006a).

Spectroscopic estimates of the metallicity of an individual star can also be obtained using the equivalent width of the Ca II triplet and the calibration relations of Rutledge et al. (1997a,b). On average, the two estimates are in good agreement for the M31 survey data (Kalirai et al. 2006a), although there is significantly larger scatter in the spectroscopic metallicity estimates due to large measurement errors in the Ca II EW measurements (Kalirai et al. 2006a; Gilbert et al. 2006). This is due primarily to the relatively low average signal-to-noise ratio of M31 RGB spectra in our spectroscopic survey (typical values of  $S/N \sim 10 \text{ pixel}^{-1}$ ). There is smaller scatter in the spectroscopic metallicity estimates and very good agreement with photometric metallicity estimates for our highest  $S/N$  M31 RGB spectra. Due to the large measurement uncertainties in the spectroscopic metallicity estimates for individual stars, we choose to use photometric metallicities for this analysis.

The use of photometric metallicities introduces systematic biases due to the isochrone set used and to the adoption of a single age and alpha-enrichment for the stellar populations. Estimates of  $[\text{Fe}/\text{H}]$  based on different sets of isochrones vary by less than 0.15 dex (Kalirai et al. 2006a). Although the alpha-enrichment of M31’s stellar halo has yet to be observationally constrained, deep HST/ACS observations of fields in M31’s stellar

<sup>8</sup> <http://astron.berkeley.edu/~cooper/deep/spec2d/primer.html>,  
<http://astron.berkeley.edu/~cooper/deep/spec1d/primer.html>

halo which reach the main sequence turnoff (e.g., Brown et al. 2006a, 2007) have shown that the stellar population of M31’s halo spans a wide range in age. In the SE shelf and H13s fields, which are contaminated by GSS debris, the stellar population ranges from 6–13 Gyr in age. The younger stars are found to be the most metal-rich, while the old population is relatively metal-poor (Brown et al. 2006b,a). In an HST/ACS M31 halo field at 21 kpc, a spread in ages of  $\sim 8$ –13 Gyr is found. Once again, the younger stars are the most metal-rich while the old stellar population is relatively metal-poor. We therefore expect our metallicity estimates to be affected mostly at the metal-rich end by the assumption of a single, old stellar population. Varying the age from 12 to 6 Gyr results in an  $\approx +0.15$  dex shift in the  $[\text{Fe}/\text{H}]$  estimates derived from isochrone fitting for metal-rich ( $[\text{Fe}/\text{H}] > -1$ ) stars (Gilbert et al. 2009).

#### 2.4. Identification of Substructure: Kinematics and Metallicity

Figure 1 presents line-of-sight velocity distributions and  $[\text{Fe}/\text{H}]$  versus line-of-sight velocity for the stars in each of six fields in which our survey of M31’s stellar halo has discovered kinematical substructure. The distributions of CMD-based  $[\text{Fe}/\text{H}]$  values (§ 2.3) in Figure 1 show the presence of a relatively metal-poor ( $[\text{Fe}/\text{H}] \lesssim -1$ ) population with a broad velocity distribution in each field, while the kinematically cold substructure tends to be relatively metal-rich ( $[\text{Fe}/\text{H}] > -1$ ). Detailed analyses of the kinematics, chemical properties, spatial distributions, and plausible origins of the various substructures are presented elsewhere [SE shelf region in Gilbert et al. (2007); a3 in Guhathakurta et al. (2006); H13s in Kalirai et al. (2006b); fields f207, H13s, a3, a13, and m4 in Gilbert et al. (2009)].

The primary signature used to identify substructure in a field is the presence of a kinematically cold population; the line-of-sight velocity distributions of these fields are inconsistent with being drawn from a single, broad Gaussian centered at M31’s systemic velocity ( $\langle v \rangle = -300$  km s $^{-1}$ ,  $\sigma_v = 129$  km s $^{-1}$ ; Gilbert et al. 2007). Fields a13 and m4 are at larger projected radial distances from the center of M31 ( $R_{\text{proj}} \sim 60$  kpc) than the study of Gilbert et al. (2007). Their line-of-sight velocity distributions are also inconsistent with being drawn from a Gaussian with parameters  $\langle v \rangle = -300$  km s $^{-1}$ ,  $\sigma_v = 100$  km s $^{-1}$ , the velocity dispersion implied for the distance of these fields by the study of Chapman et al. (2006).

The velocity distribution in each field has been fit by a combination of Gaussians using a maximum-likelihood technique (red curves in Figure 1). In general, the number of Gaussians used in the multi-Gaussian fits is the minimum required to produce a maximum-likelihood fit that is consistent with the data, although additional evidence of substructure in a field is also taken into account in determining the number of kinematical components in a given spectroscopic field (Gilbert et al. 2007, 2009). The Gaussian components of the underlying kinematically hot population were held fixed ( $\langle v \rangle^{\text{sp}} = -300$  km s $^{-1}$ ,  $\sigma_v^{\text{sp}} = 129$  km s $^{-1}$ ) while the properties of the Gaussians representing the kinematically cold populations (mean velocity and velocity dispersion) and the

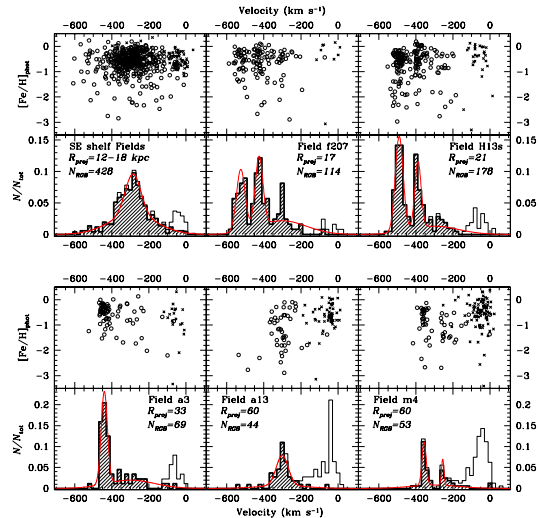


FIG. 1.— Line-of-sight velocity distributions and  $[\text{Fe}/\text{H}]$  versus line-of-sight velocity for the fields discussed in this paper. Shaded velocity histograms and open circles represent stars classified as M31 red giants by the Gilbert et al. (2006) diagnostic method, while crosses represent stars classified as MW dwarfs. Open velocity histograms show the velocity distribution of all the stars (M31 RGB and MW dwarf) in our fields. The solid curves show the best-fit velocity distributions in each field (§ 2.4). In general, the observed kinematically cold populations are more metal-rich than the rest of the stellar population.

TABLE 2  
FRACTION OF M31 RGB STARS IN KINEMATICALLY COLD COMPONENTS.

Field	$\langle v \rangle^{\text{KCC}}$ (km s $^{-1}$ )	$N_{\text{KCC}}/N_{\text{tot}}^{\text{a}}$
SE shelf	-285	$0.41^{+0.10}_{-0.09}$
f207	-524	$0.31^{+0.08}_{-0.07}$
f207	-426	$0.31^{+0.11}_{-0.10}$
H13s	-490	$0.48^{+0.07}_{-0.06}$
H13s	-388	$0.27^{+0.07}_{-0.08}$
a3	-441	$0.59^{+0.11}_{-0.12}$
a13	-301	$0.72^{+0.15}_{-0.21}$
m4	-355	$0.45^{+0.14}_{-0.13}$
m4	-255	$0.16^{+0.10}_{-0.08}$

<sup>a</sup>Quoted errors are the 90% confidence limits from the maximum likelihood analysis (§ 2.4).

fraction of stars in each cold population were allowed to vary. The SE shelf, f207, H13s, a3, and a13 fields all contain substructure related to the GSS in M31 (Kalirai et al. 2006b; Guhathakurta et al. 2006; Gilbert et al. 2007, 2009). Fields f207 and H13s both have a second kinematically cold component which may be unrelated to the GSS. The cold components with mean velocities of  $-527$  km s $^{-1}$  and  $-490$  km s $^{-1}$  in f207 and H13s, respectively, are those associated with the GSS (Gilbert et al. 2009). Although there are some lines of evidence that suggest the substructure in m4 and the secondary substructures in fields f207 and H13s may also be associated with the GSS (Fardal et al. 2008; Gilbert et al. 2009), the origins of these features are currently unknown.

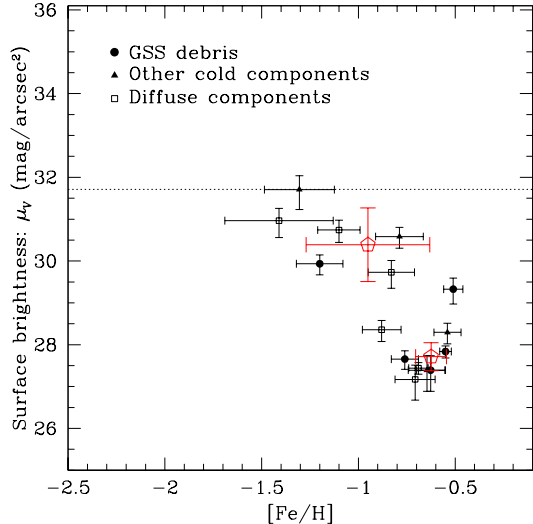


FIG. 2.— Surface brightness versus average metallicity for each of the kinematical components in Figure 1: kinematically cold components likely associated with the GSS (solid circles), kinematically cold components which are not known to be associated with the GSS (solid triangles), and the kinematically hot components (open squares). The error bars represent the Poisson error for the surface brightness estimates and the error in the mean  $[\text{Fe}/\text{H}]$  value. The mean and root-mean-square (rms)  $[\text{Fe}/\text{H}]$  and  $\mu_V$  of the lower surface brightness ( $\mu_V > 29$  mag arcsec $^{-2}$ ) and higher surface brightness features ( $\mu_V < 29$  mag arcsec $^{-2}$ ) kinematically cold components are also shown (open hexagons and error bars). Higher surface brightness features are on average more metal-rich than lower surface brightness features, and kinematically cold substructures are on average more metal-rich than the kinematically hot populations. Lower surface brightness features display a larger spread in metallicity than higher surface brightness features. The dotted line denotes the faintest identifiable tidal streams to date, given the number of stars in our DEIMOS survey.

### 2.5. Characteristics of Observed Substructure: Surface Brightness versus Metallicity

Figure 2 displays surface brightness versus mean metallicity for the M31 stellar halo data presented in Figure 1. Each kinematical component identified in the 6 fields shown in Figure 1 is represented: the kinematically cold components related to the GSS (solid circles), the kinematically cold components that are not known to be associated with the GSS (solid triangles), and the kinematically hot population (open squares).

Table 2 lists the maximum-likelihood fraction of M31 RGB stars in each of the kinematically cold components (from the fits shown in Fig. 1). These fractions were used to determine the number of M31 RGB stars in each component. The ratio of M31 RGB to MW dwarf stars, multiplied by the expected number of MW dwarf stars along the line of sight to each field (based on the Besancon Galactic population model; Robin et al. 2003) is used to estimate the surface brightness of each component, as described in Guhathakurta et al. (2005). Correction factors that account for the rate of successful velocity measurements as a function of magnitude and varying M31 RGB target efficiency due to photometric pre-selection of stars likely to be red giants are applied to each field (Gilbert et al., in preparation). The spectroscopic surface brightness estimates are normalized using photometric surface brightness estimates from Pritchett & van den

Bergh (1994). Error bars represent Poisson error estimates based on the number of stars in each component.

The  $[\text{Fe}/\text{H}]$  for the kinematically cold components is the mean  $[\text{Fe}/\text{H}]$  of stars within  $\pm 2\sigma_v$  of the mean velocity of the cold component ( $|v_{\text{star}} - \langle v \rangle^{\text{KCC}}| < 2\sigma_v^{\text{KCC}}$ ), while the  $[\text{Fe}/\text{H}]$  for the kinematically hot components is the mean  $[\text{Fe}/\text{H}]$  of stars with velocities greater than  $2\sigma_v^{\text{KCC}}$  from the mean velocity of the cold components ( $|v_{\text{star}} - \langle v \rangle^{\text{KCC}}| > 2\sigma_v^{\text{KCC}}$ ; in fields with two cold components, stars must meet this criterion for both). The numbers of stars which are thus used for the  $[\text{Fe}/\text{H}]$  measurement for each component are consistent with the number of stars expected to be in each component based on the maximum-likelihood fits shown in Figure 1. Error bars represent the error in the mean  $[\text{Fe}/\text{H}]$  value.

Since stars cannot be identified individually as belonging to a particular kinematical component, these velocity cuts are chosen to maximize the number of stars involved in the  $[\text{Fe}/\text{H}]$  measurement of the kinematically cold component, while minimizing contamination in the mean  $[\text{Fe}/\text{H}]$  measurement from other kinematical components. Even so, the metallicity estimate of the substructure will be biased by contamination from the kinematically hot component. This effect will be greatest for the least dominant substructures, and will in general bias the mean metallicity of the kinematically cold substructures to lower values. In the SE shelf fields, where we have a large statistical sample, accounting for the contamination by the kinematically hot component in the measurement of the mean metallicity of the kinematically cold component changes the mean metallicity by only +0.03 dex (Gilbert et al. 2007); however, it must be noted that the  $[\text{Fe}/\text{H}]$  distribution of the kinematically hot population in the SE shelf fields is very similar to the  $[\text{Fe}/\text{H}]$  distribution of the kinematically cold population.

The assumption of a single, old stellar population likely provides a larger source of systematic error in the photometric (CMD-based) metallicity estimates. As discussed in § 2.3, this assumption is known to be wrong for at least some of our fields and is expected to affect our metallicity estimates mostly on the metal-rich end. Indeed, a comparison of the mean Ca II-based spectroscopic metallicity estimates (measured in bins of photometric metallicity) of stars associated with the kinematically hot and cold populations shows that the kinematically cold populations do, on average, have a higher spectroscopic abundance than the kinematically hot population at a given photometric abundance. This indicates that the substructure in M31’s stellar halo is on average younger and/or more enriched in  $[\alpha/\text{Fe}]$  than M31’s kinematically smooth stellar halo. Using 6 Gyr instead of 12 Gyr isochrones changes the  $[\text{Fe}/\text{H}]$  estimates by  $\sim +0.15$  for more metal-rich stars ( $[\text{Fe}/\text{H}] \gtrsim -1.0$ ) and by as much as  $\sim +0.3$  for metal-poor stars ( $[\text{Fe}/\text{H}] \lesssim -1.5$ ). Thus, the true metallicity spread is likely greater than Figure 2 suggests.

The data in Figure 2 show a clear correlation between surface brightness and metallicity: higher surface brightness features are more metal-rich than lower surface brightness features. The kinematically cold substructures are on average more metal-rich than the underlying kinematically hot components, as was implied in Figure 1. Figure 2 also shows evidence for a larger spread

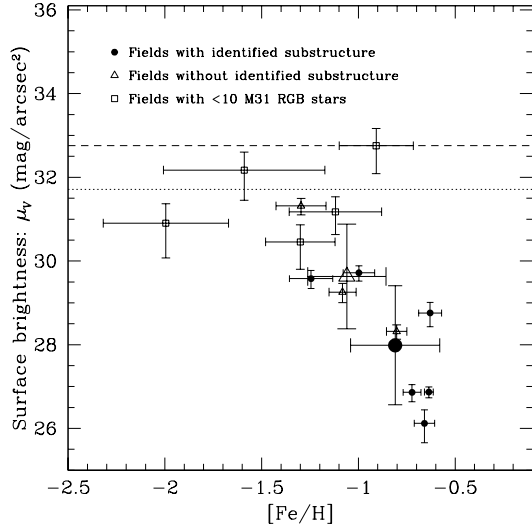


FIG. 3.— The same as Figure 2 but for entire fields from our M31 spectroscopic survey. Fields are divided into three categories: fields with (solid circles; Fig. 1) and without (open triangles) kinematically identified substructure, and fields with small numbers of M31 RGB stars ( $\lesssim 10$ ), for which we cannot determine if substructure is present. The large symbols show the mean and rms (errorbars)  $[\text{Fe}/\text{H}]$  and  $\mu_V$  of fields with and without identified substructure. Fields with identified substructure are on average more metal-rich than fields without identified substructure. The dashed line represents the current surface brightness limit achieved in our M31 spectroscopic survey, while the dotted line denotes the faintest tidal stream identified in our survey (Fig. 2).

in metallicities among lower surface brightness features ( $\mu_V > 29$  mag arcsec $^{-2}$ ) than higher surface brightness features ( $\mu_V < 29$  mag arcsec $^{-2}$ ). The root-mean-square (rms) deviation of average  $[\text{Fe}/\text{H}]$  values among higher surface brightness, kinematically cold components is only 0.08 dex, while the rms deviation of average  $[\text{Fe}/\text{H}]$  values among lower surface brightness, kinematically cold components is 0.32 dex.

Figure 3 displays surface brightness versus mean metallicity for fields from our M31 halo spectroscopic survey with kinematically-identified substructure (those presented in Figure 1; solid circles), fields without kinematically-identified substructure (open triangles), and fields for which we cannot determine if substructure is present due to small numbers of M31 RGB stars ( $\lesssim 10$  M31 stars per field; open squares). The fields with small numbers of M31 RGB stars are all located in the outer regions of M31’s stellar halo ( $R_{\text{proj}} \gtrsim 80$  kpc), while the fields without kinematically-identified substructure span a similar range in projected distance from M31’s center as the fields with kinematically-identified substructure. Fields with identified substructure are on average more metal-rich than fields without identified substructure, as would be expected if kinematically cold substructures are more metal-rich on average than the kinematically hot population (Fig. 2).

### 3. SIMULATED STELLAR HALOS

Simulations of hierarchical stellar halo formation provide a physical explanation of the surface brightness versus metallicity trend observed in our M31 halo data. In this section, we briefly describe the simulations (§3.1), present the abundance properties of substructure in the

simulated stellar halos (§3.2), and discuss the physical mechanisms behind the trends (§3.3). We will compare the abundance trends in the simulations with our M31 observations in §4.

#### 3.1. Methods

The BJ05 simulations follow the formation of 11 MW-analog stellar halos via accretion in a cosmological context. For each host halo, a merger tree was generated using the extended Press-Schechter formalism (Somerville & Kolatt 1999; Lacey & Cole 1993). Only merger histories without recent high-mass mergers were selected, resulting in  $z = 0$  halos suitable for hosting a large disk galaxy like the Milky Way or M31. For each merger, an  $N$ -body simulation was used to track the evolution of the dark matter halo of the satellite galaxy in the host halo potential. The potential of the host galaxy is modeled with a smoothly growing, analytic function, and satellite-satellite interactions are neglected. Overall, these assumptions will lead to an unnatural enhancement of the level of substructure in the simulated halos, especially in the inner halo. Thus, in the following analysis we discuss only the properties of the simulated stellar halos exterior to  $R = 20$  kpc.

Gas accretion onto each satellite halo tracks its mass accretion history and the star formation rate within each object is proportional to its instantaneous gas content over a fixed timescale. The timescale is chosen so that dwarfs infalling today would contain similar gas fractions to those observed in Local Group field objects (see BJ05 for details). Given the gas infall, star formation rates, and mass of a satellite as a function of time, the method of Robertson et al. (2005) is used to follow the chemical evolution of the stellar populations (see also Font et al. 2006b). The Robertson et al. (2005) prescriptions include enrichment from Type Ia and Type II supernovae and the effects of feedback (from supernovae and stellar winds). The free parameters in the prescriptions are constrained by requiring consistency with observations: the Fe and  $\alpha$ -element wind efficiencies are chosen separately by requiring matches to the observed stellar mass-metallicity relation for dwarf galaxies (e.g., Larson 1974; Mateo 1998; Dekel & Woo 2003) and the  $\alpha$ -element abundance patterns in satellite dwarf spheroidals (e.g. Venn et al. 2004). Both gas accretion and star formation are assumed to truncate once the satellite is accreted onto the host halo. A variable mass-to-light ratio is assigned to every dark matter particle in order to embed the stellar components within the dark matter halos of the satellites in a way that reproduces the observed distribution of structural properties of Local Group dwarfs. Each stellar particle in the simulations is randomly assigned  $[\text{Fe}/\text{H}]$  and  $[\alpha/\text{Fe}]$  ratios based on the satellite’s star formation history (Font et al. 2006b). Thus each model satellite contains a realistic intrinsic metallicity spread, but no radial metallicity gradient.

The resulting simulated halos have similar luminosities and stellar density profiles to the Milky Way’s halo, and the surviving satellites are comparable in number, luminosity distribution, and structural properties to those of the Milky Way (discovered prior to 2005). The models are also able to reproduce the observed difference in  $[\alpha/\text{Fe}]$  ratios between the Milky Way’s stellar halo and dwarf satellites. The lower  $[\alpha/\text{Fe}]$  ratios in the surviving

simulated dwarf galaxies are due to their late accretion times and the prolonged, less bursty star formation histories of these systems compared with those of the progenitors of the halo (Robertson et al. 2005; Font et al. 2006a). In the models, the kinematically cold streams tend to have distinct chemical abundances (i.e. higher  $[\text{Fe}/\text{H}]$  and lower  $[\alpha/\text{Fe}]$ ) than that of the smooth, more well-mixed halo (Font et al. 2006b). This is also due to the fact that the progenitors of these streams were accreted following the formation of the bulk of the halo.

Of course, in the framework of the hierarchical formation of stellar halos, there is no clear demarcation between tidal streams and the “smooth” halo. In reality, present day stellar halos are expected to display a natural progression in the kinematical properties of their unbound substructure, ranging from thin and kinematically cold to more disperse, kinematically hot substructure. In light of the above findings, the prospect of using chemical abundances as a complementary dimension to phase-space to disentangle various substructures is encouraging.

### 3.2. Predicted Abundance Properties of Substructure

Figure 4 shows the projected surface brightness (*top*), metallicities (*middle*), and alpha-enrichment (*bottom*) for two of the BJ05 simulated stellar halos. The projected surface brightness reflects the total luminosity in each  $0.25 \text{ kpc} \times 0.25 \text{ kpc}$  pixel, summed over all the stellar populations. The  $[\text{Fe}/\text{H}]$  and  $[\alpha/\text{Fe}]$  values are the stellar-mass-weighted average of the stellar populations in each pixel. These maps reveal that the highest surface brightness streams tend to be more metal-rich and less alpha-enhanced than the lower surface brightness streams.

This is demonstrated quantitatively in Figure 5, which displays maximum surface brightness versus mean metallicity (*left panels*) and alpha-enhancement (*right panels*) for individual stellar streams produced by accretion events in all 11 BJ05 stellar halos, taken from the analysis of Johnston et al. (2008). Only stellar streams that contribute at least 50% of the total light in the halo at the position of their highest surface brightness point and which are at radial distances greater than 30 kpc from the center of the galaxy are included. Although for any given maximum surface brightness stellar streams exhibit a range of mean  $[\text{Fe}/\text{H}]$  and  $[\alpha/\text{Fe}]$  values, the higher surface brightness streams are in general more metal-rich and less alpha-enhanced than the lower surface brightness streams.

### 3.3. Physical Interpretation

The points in Figure 5 are color-coded by mass of the progenitor satellite (*top panels*) and time of accretion of the progenitor satellite onto the host halo (*bottom panels*; see figure caption for details). The top left panel clearly shows the effect of the assumption of a mass-metallicity relation for the progenitor satellites (based on observations of dwarf galaxies; §3.1): more massive satellites are more metal-rich, thus the tidal streams produced as massive satellites fall into the host halo are also more metal-rich. Since the more massive progenitors also typically produce brighter stellar streams, it follows that the surface brightness and metallicity of stellar streams are correlated.

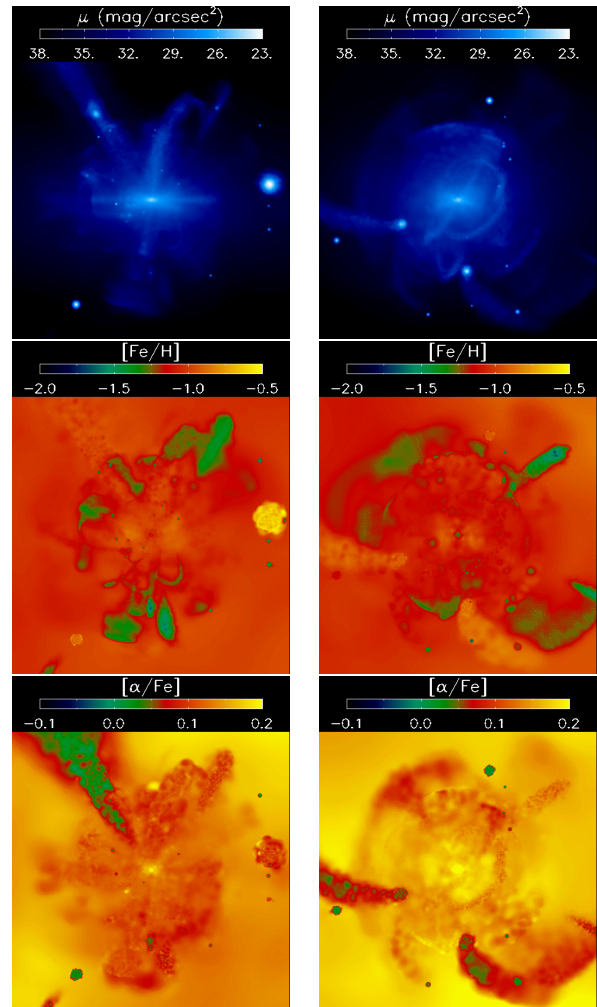


FIG. 4.— Maps of projected surface brightness (*top*), average metallicity (*middle*), and average alpha-enrichment (*bottom*) for 2 of the BJ05 simulated stellar halos. Each map depicts a  $300 \times 300 \text{ kpc}$  region. The  $[\text{Fe}/\text{H}]$  and  $[\alpha/\text{Fe}]$  values are the stellar-mass-weighted average of all the stars in each pixel. A comparison of the surface brightness and metallicity maps reveals that the brightest features tend to be more metal-rich and less alpha-enhanced than the rest of the halo. Image credit: Sanjib Sharma.

The alpha-enhancement of the stellar streams traces the time of accretion of the progenitor onto the host halo, as is demonstrated in the bottom right panel of Figure 5. Alpha elements are produced in Type II supernovae; their abundances become subsequently diluted by the elements produced in Type I supernovae. Thus, progenitors accreted early are alpha-enriched relative to progenitors that are accreted later and have had longer star formation histories. The surface brightness of stellar streams observed today is a function not only of the mass of the progenitor but also of the time since accretion, therefore the bottom right panel shows a slight trend for stellar streams produced by progenitors that were accreted at early times to have lower surface brightnesses than progenitors that were accreted at later times. This leads to the anti-correlation between surface brightness and alpha-enrichment.

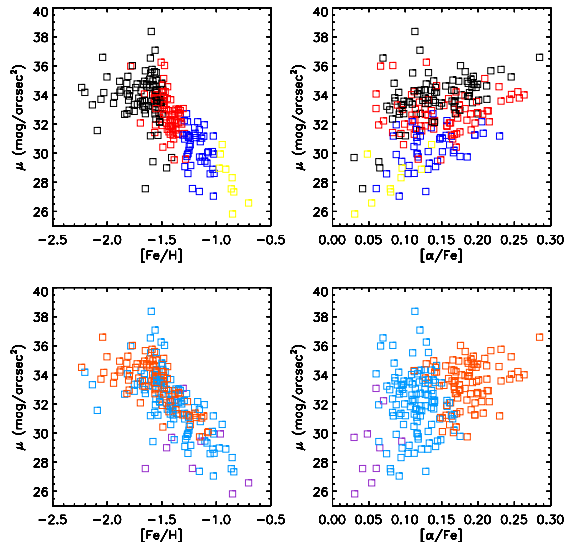


FIG. 5.— Maximum surface brightness versus average metallicity (*left panels*) and alpha enhancement (*right panels*) for stellar streams in the 11 BJ05 simulated stellar halos. The top panels are color coded according to the luminosity of the progenitor satellite [ $L < 10^6 L_{\odot}$  (*black*);  $10^6 L_{\odot} < L < 10^7 L_{\odot}$  (*red*);  $10^7 L_{\odot} < L < 10^8 L_{\odot}$  (*blue*);  $10^8 L_{\odot} < L < 10^9 L_{\odot}$  (*yellow*)] while the bottom panels are color coded according to the time of accretion of the progenitor satellite onto the host halo [ $3 < t_{\text{acc}} < 6$  Gyr (*purple*);  $6 < t_{\text{acc}} < 9$  Gyr (*cyan*);  $9 < t_{\text{acc}} < 12$  Gyr (*orange*)]. The distribution in the left panels is a reflection of the mass-metallicity relationship observed for Local Group dwarfs, while the distribution in the right panels reflects the time-sensitivity of alpha elements. The bottom panels also show a slight tendency for more recent accretion events to be brighter.

## 4. COMPARISON OF OBSERVATIONS AND SIMULATIONS

### 4.1. Observing the Simulations

Figure 5 provides useful insight into the physical mechanisms underlying the expected general relationships between the chemical enrichment and maximum surface brightness of stellar streams. The data in Figure 2 appear to agree qualitatively with the characteristics seen in the left panels of Figure 5; identifiable (and thus fairly dominant and high surface brightness) substructures tend to be relatively metal-rich. However, our Keck/DEIMOS spectroscopic masks provide information on the characteristics of the population in isolated lines-of-sight through M31’s stellar halo, rather than global information about individual streams. The data cannot be compared directly with Figure 5, since the maximum surface brightness of an observed stellar stream can only be determined by tracing the full extent of the stream in space. The only stellar stream for which this measurement could currently be made in M31 is the GSS.

A more direct comparison between the data and simulations can be made by analyzing stellar populations along individual lines-of-sight through the simulated stellar halos. Figure 6 displays mean stellar metallicity and alpha-enhancement as a function of surface brightness for sight lines through one of the BJ05 simulated stellar halos; each point represents a line-of-sight that covers a projected area of  $0.4 \text{ kpc} \times 0.4 \text{ kpc}$ . Only lines of sight beyond 20 kpc in projection from the center of the galaxy are included (§ 3.1). Lines-of-sight through the simulated stellar halos whose stellar populations are dominated by

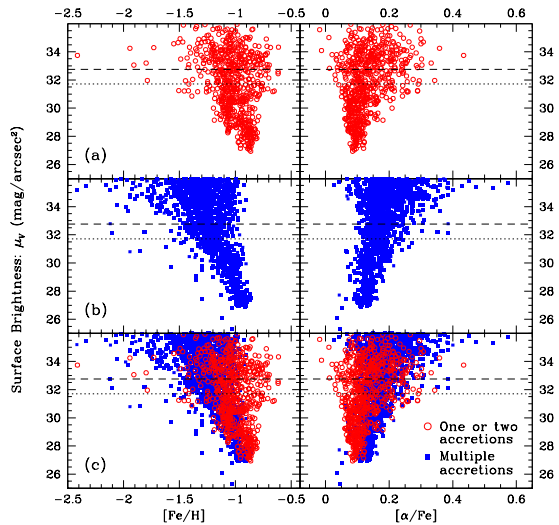


FIG. 6.— Surface brightness versus stellar-mass-weighted average metallicity (*left*) and alpha-enhancement (*right*) for individual lines-of-sight through one of the 11 BJ05 simulated stellar halos, divided into two categories based on the number and prominence of individual stellar streams. (a) Lines-of-sight where the majority of the stellar population derives from one or two accretion events (solid red circles). (b) Lines-of-sight where the majority of the stellar population derives from multiple ( $\geq 3$ ) accretion events (open blue squares). (c) The two types of sight-lines superimposed. The overall trends of surface brightness with metallicity and alpha-enhancement (panel c), are similar to those in Figure 5, although with a somewhat steeper slope. For a given surface brightness, lines-of-sight whose stellar populations are dominated by debris from one or two accretion events are on average more metal-rich and less alpha-enhanced than lines-of-sight whose stellar populations are composed primarily by debris from multiple accretion events. The surface brightness of the faintest tidal debris that has been identified as kinematically cold substructure in our Keck/DEIMOS survey is denoted by the dotted line (Fig. 2) while the current surface brightness limit of our spectroscopic survey is denoted by the dashed line (Fig. 3).

debris from one or two accretion events are denoted by red solid circles in Figure 6, while lines-of-sight whose stellar populations are largely comprised of debris from multiple ( $\geq 3$ ) accretion events are denoted by blue open squares.

The same general trends seen in individual streams (Fig. 5) are repeated here, with a steeper slope: higher surface brightness lines-of-sight are on average more metal-rich and less alpha-enhanced than lines-of-sight of lower surface brightness. The same physical mechanisms discussed in § 3.3 are relevant here, however each point in Figure 6 is averaging over stellar populations from *multiple* satellite progenitors. Thus, the trends in metallicity and alpha-enhancement with surface brightness are not as strong.

### 4.2. Common Trends

We can’t know a priori the number of streams that are along any particular observed sight-line in M31’s stellar halo. However, separating the kinematically cold and hot components in fields with identifiable substructure, as is done in Figure 2, effectively separates a single field into the equivalents of lines-of-sight dominated by stellar populations arising from a single accretion event (kinematically cold components) and lines of sight dominated by stellar populations arising from many accretion events

(kinematically hot components). In a stellar halo built in a purely dissipationless fashion, a population with a large spread in velocities is most likely to be formed from the superposition of debris originating in multiple satellites that merged early with the host galaxy. The dotted line in Figure 6 denotes the surface brightness of the faintest tidal debris that is identifiable as kinematically cold substructure in our Keck/DEIMOS survey (Fig. 2).

The simulations (Fig. 6) show the same general trends seen in our M31 data (Fig. 2): (1) Higher surface brightness features are on average more metal-rich, and (2) at a given surface brightness lines-of-sight dominated by debris from one or two accretion events tend to be more metal-rich than those dominated by debris from multiple accretion events.

We have discussed the first trend in §§3.2–3.3, and shown that in a stellar halo formed via accretion, it can be explained via the mass-metallicity relationship for dwarf galaxies: larger galaxies are more metal-rich and also produce the brightest tidal streams.

This same physical mechanism can also explain the second trend. In order for tidal debris from a single satellite to dominate the stellar population in a line-of-sight through a halo, the tidal debris must be part of a particularly bright stellar stream relative to the average surface brightness at its location in the halo. It thus must originate from a relatively massive satellite (relatively metal-rich) and/or recent accretion event (low relative  $\alpha$ -enhancement) compared to the accretion events in a line-of-sight of equivalent surface brightness but composed primarily of debris from multiple progenitors.

With multiple physical mechanisms (e.g., the size and orbit of the progenitor and the time since its accretion onto the host halo) affecting the surface brightness of individual streams, a significant spread in the chemical properties of individual sight-lines of a given surface brightness, as seen in Figure 6, is to be expected. This is particularly relevant for faint lines-of-sight, since faint stellar streams can be formed by the recent accretion of a low mass progenitor or early accretion events whose debris streams have spatially dissipated, or both. The brightest lines of sight, however, must be composed of debris from very massive and/or recent events, resulting in a narrower range in chemical properties.

The data also show evidence of a narrower spread in metallicity among higher surface brightness streams/lines-of-sight and a larger spread in metallicity among fainter streams/lines-of-sight (Figs. 2 & 3, §2.5). The rms deviation of mean  $[\text{Fe}/\text{H}]$  values for the high surface brightness ( $\mu_V < 29$  mag arcsec $^{-2}$ ) and low surface brightness ( $\mu_V > 29$  mag arcsec $^{-2}$ ) tidal streams observed in our M31 spectroscopic data are 0.08 dex and 0.32 dex, respectively (although the observed spread is likely underestimated due to systematic errors, §2.5). To compare the spread in  $[\text{Fe}/\text{H}]$  seen in the observations with that seen in the simulations, we impose surface brightness limits on the simulations based on the surface brightness of tidal streams observed in our survey (Fig. 2), and measure the rms deviation of the mean  $[\text{Fe}/\text{H}]$  values of lines-of-sight through the BJ05 simulated stellar halo which have a stellar population dominated by one or two accretion events (open circles in Fig. 6). The rms deviation of  $[\text{Fe}/\text{H}]$  values

for high surface brightness lines-of-sight ( $27 < \mu_V < 29$  mag arcsec $^{-2}$ ) is 0.07 dex, while the rms deviation of  $[\text{Fe}/\text{H}]$  values for low surface brightness lines-of-sight ( $29 < \mu_V < 31.7$  mag arcsec $^{-2}$ ) is 0.13 dex. The spread in  $[\text{Fe}/\text{H}]$  values in our observations and the simulations is similar for high surface brightness lines-of-sight, while the spread in  $[\text{Fe}/\text{H}]$  values in the observations is greater than in the simulations for lower surface brightness lines-of-sight. The rms deviation of  $[\alpha/\text{Fe}]$  values in the simulations for the magnitude limits used above are 0.02 dex and 0.05 dex, respectively.

We note that the absolute  $[\text{Fe}/\text{H}]$  scale is uncertain for both the observations (due to the age-metallicity degeneracy of the RGB as well as systematic errors in the generation of theoretical isochrones, §2.3) and the simulations (where the output  $[\text{Fe}/\text{H}]$  is dependent on the input chemical enrichment prescriptions, §3.1). Therefore, we do not attempt to directly compare the metallicities of the data and simulations.

#### 4.3. Discussion

The common trend of increasing metallicity with increasing surface brightness in lines-of-sight through M31’s stellar halo and simulated stellar halos is encouraging. It gives us confidence that such simulations can lead to meaningful interpretation of stellar halo observations.

The surface brightness of M31’s stellar halo is observed to decrease with increasing distance from the center of the galaxy (Guhathakurta et al. 2005; Irwin et al. 2005; Ibata et al. 2007), and the inner region of M31’s stellar halo is observed to be more metal-rich than the outer region (Kalirai et al. 2006a; Chapman et al. 2006; Koch et al. 2008). Thus, the general increase in mean  $[\text{Fe}/\text{H}]$  with increasing surface brightness of the kinematically broad components in our M31 data (Fig. 2, open squares) is expected. In the hierarchical framework, this global trend in stellar halo metallicity could be explained with the same physical mechanisms invoked above (§4.2). Although the radial extent over which tidal debris from an individual accretion event is spread depends on the orbit of the progenitor, the effect of dynamical friction on the progenitor’s orbit is more important for more massive progenitors, causing them to sink to the center of the gravitational potential of the host galaxy more quickly than less massive progenitors. Therefore, more massive progenitors will tend to deposit most of their relatively metal-rich debris in the interior regions of the host halo.

If the number of M31 stars detected in an observational field is small ( $\lesssim 20$ ), it can be difficult to determine if the field is dominated by contributions from one or two kinematical components or if the field contains contributions from multiple kinematical components (i.e., contains a relatively hot population). The results of the simulations can be used to examine the probable number of stellar streams in a given field. If the mean  $[\text{Fe}/\text{H}]$  of a field is relatively high compared to other fields of comparable surface brightness, the field may be dominated by one or two stellar streams, while if the mean  $[\text{Fe}/\text{H}]$  is relatively low, the field is more likely to be dominated by multiple superposed stellar streams along the line of sight (i.e., the stellar population along the line of sight is approaching a dynamically hot population).

There are several fields in our M31 spectroscopic survey in which we have spectra of  $\lesssim 10$  M31 RGB stars (open squares, Fig. 3); all are in M31's sparse outer halo ( $R_{\text{proj}} \gtrsim 80$  kpc). Based on the above discussion (§ 4.2), the outer halo fields with the highest mean  $[\text{Fe}/\text{H}]$  values are the most likely to be dominated by debris from one or two high mass progenitors, while the fields with lower mean  $[\text{Fe}/\text{H}]$  are more likely to be dominated by debris from many lower mass progenitors. Future observations will be able to test this conjecture. If fields with lower mean  $[\text{Fe}/\text{H}]$  are found to have stars with a wide range of velocities, it will support the hypothesis that the field is dominated by debris from many progenitors. Although the presence of a significant old, metal-poor stellar population in a higher mass progenitor may somewhat obscure this effect, the mean  $[\text{Fe}/\text{H}]$  of a field dominated by such a progenitor would still be expected to be higher on average than the mean  $[\text{Fe}/\text{H}]$  of a field dominated by low mass progenitors which did not have an appreciable number of metal-rich stars.

There are currently no observational constraints on the alpha-enrichment of stars in M31's stellar halo. However, if a mean  $[\alpha/\text{Fe}]$  can be measured for the M31 RGB stars in a given field (i.e., by measuring the relative abundances of elements in a composite spectrum formed by coaddition of spectra from multiple stars), it could be used to constrain the average time of accretion of the stellar population. Measurement of the mean  $[\alpha/\text{Fe}]$  would greatly facilitate the interpretation of the surface brightness of specific fields by lessening the degeneracy between the effect of the luminosity of accreted satellites versus the time of accretion onto the host halo.

## 5. SUMMARY

We have presented the general trends of surface brightness with chemical enrichment of RGB stars observed in the course of our M31 Keck/DEIMOS spectroscopic survey and of stellar streams in simulations of stellar halos formed in a hierarchical framework. Kinematically identified substructure in M31's stellar halo is metal-rich relative to the kinematically hot population, and higher surface brightness features are more metal-rich than lower surface brightness features.

Similar trends are found in the simulated BJ05 stellar halos, which are formed entirely via accretion. Higher surface brightness lines-of-sight through the simulated stellar halos are in general more metal-rich than lower

surface brightness lines-of-sight, and lines-of-sight dominated by stars from one or two accretion events are in general more metal-rich than lines-of-sight whose stars come from many events. The comparison of the observations and simulations provides a physical explanation for the observed trends in surface brightness and metallicity of stellar halo structure: more massive progenitors, which are also the most metal-rich, produce the brightest stellar halo substructures. This results in the dominance of metal-rich streams in galactic halos.

Both the data and the simulation results show a significant spread in metallicity at a given surface brightness for lines-of-sight through stellar halos. This is a result of the varying time since accretion of the tidal streams' progenitors onto the host halo. Tidal streams produced by more recent accretion events are, on average, brighter than tidal streams produced by less recent accretion events.

The simulations show a relationship between the alpha-enhancement and surface brightness of tidal streams is expected: fainter tidal debris is on average more alpha-enhanced than brighter tidal debris. This arises from the different times of accretion of progenitor satellites onto the host halo, as well as the assumption of the truncation of star formation upon accretion onto the host halo. Satellites accreted early had less time for chemical enrichment via Type Ia SNe to reduce their alpha enrichment, while their tidal debris has had more time to spread along the progenitor's orbit within the host halo. The ability to measure the alpha-enrichment of M31 RGB stars would thus lead to constraints on both the luminosity and the time of accretion onto the host halo of the progenitors of M31's tidal streams.

The authors would like to thank James Bullock, Brant Robertson, Steve Majewski, Marla Geha, and Sanjib Sharma for their contributions to the research programs whose products were used in this work. The authors of the paper benefited from the hospitality of the Aspen Center for Physics in June 2006. This work was supported by NSF grants AST-0307966, AST-0507483, and AST-0607852 (K.M.G., P.G.) and a UCSC Chancellor's Division Dissertation-Year Fellowship (K.M.G.), NSF CAREER award AST-0733966 and NSF grant AST-0734864 (K.V.J.), and an STFC Fellowship at the Institute for Computational Cosmology in Durham (A.S.F.).

## REFERENCES

- Battaglia, G., Helmi, A., Morrison, H., Harding, P., Olszewski, E. W., Mateo, M., Freeman, K. C., Norris, J., & Shectman, S. A. 2005, *MNRAS*, 364, 433
- Bell, E. F., Zucker, D. B., Belokurov, V., Sharma, S., Johnstone, K. V., Bullock, J. S., Hogg, D. W., Jahnke, K., de Jong, J. T. A., Beers, T. C., Evans, N. W., Grebel, E. K., Ivezić, Ž., Koposov, S. E., Rix, H.-W., Schneider, D. P., Steinmetz, M., & Zolotov, A. 2008, *ApJ*, 680, 295
- Belokurov, V., Evans, N. W., Irwin, M. J., Lynden-Bell, D., Yanny, B., Vidrih, S., Gilmore, G., Seabroke, G., Zucker, D. B., Wilkinson, M. I., Hewett, P. C., Bramich, D. M., Fellhauer, M., Newberg, H. J., Wyse, R. F. G., Beers, T. C., Bell, E. F., Barentine, J. C., Brinkmann, J., Cole, N., Pan, K., & York, D. G. 2007, *ApJ*, 658, 337
- Belokurov, V., Zucker, D. B., Evans, N. W., Gilmore, G., Vidrih, S., Bramich, D. M., Newberg, H. J., Wyse, R. F. G., Irwin, M. J., Fellhauer, M., Hewett, P. C., Walton, N. A., Wilkinson, M. I., Cole, N., Yanny, B., Rockosi, C. M., Beers, T. C., Bell, E. F., Brinkmann, J., Ivezić, Ž., & Lupton, R. 2006, *ApJ*, 642, L137
- Bertin, E., & Arnouts, S. 1996, *A&AS*, 117, 393
- Brown, T. M., Ferguson, H. C., Smith, E., Kimble, R. A., Sweigart, A. V., Renzini, A., Rich, R. M., & VandenBerg, D. A. 2003, *ApJ*, 592, L17
- Brown, T. M., Smith, E., Ferguson, H. C., Guhathakurta, P., Kalirai, J. S., Rich, R. M., Renzini, A., Sweigart, A. V., Reitzel, D., Gilbert, K. M., & Geha, M. 2007, *ApJ*, 658, L95
- Brown, T. M., Smith, E., Ferguson, H. C., Rich, R. M., Guhathakurta, P., Renzini, A., Sweigart, A. V., & Kimble, R. A. 2006a, *ApJ*, 652, 323
- Brown, T. M., Smith, E., Guhathakurta, P., Rich, R. M., Ferguson, H. C., Renzini, A., Sweigart, A. V., & Kimble, R. A. 2006b, *ApJ*, 636, L89

- Bullock, J. S., & Johnston, K. V. 2005, *ApJ*, 635, 931
- Bullock, J. S., Kravtsov, A. V., & Weinberg, D. H. 2001, *ApJ*, 548, 33
- Chapman, S. C., Ibata, R., Irwin, M., Koch, A., Letarte, B., Martin, N., Collins, M., Lewis, G. F., McConnachie, A., Peñarrubia, J., Rich, R. M., Trethewey, D., Ferguson, A., Huxor, A., & Tanvir, N. 2008, *MNRAS*, 390, 1437
- Chapman, S. C., Ibata, R., Lewis, G. F., Ferguson, A. M. N., Irwin, M., McConnachie, A., & Tanvir, N. 2006, *ApJ*, 653, 255
- Dekel, A., & Woo, J. 2003, *MNRAS*, 344, 1131
- Fardal, M. A., Babul, A., Guhathakurta, P., Gilbert, K. M., & Dodge, C. 2008, *ApJ*, 682, L33
- Fardal, M. A., Guhathakurta, P., Babul, A., & McConnachie, A. W. 2007, *MNRAS*, 380, 15
- Font, A. S., Johnston, K. V., Bullock, J. S., & Robertson, B. E. 2006a, *ApJ*, 638, 585
- , 2006b, *ApJ*, 646, 886
- Font, A. S., Johnston, K. V., Ferguson, A. M. N., Bullock, J. S., Robertson, B. E., Tumlinson, J., & Guhathakurta, P. 2008, *ApJ*, 673, 215
- Gilbert, K. M., Fardal, M., Kalirai, J. S., Guhathakurta, P., Geha, M. C., Isler, J., Majewski, S. R., Ostheimer, J. C., Patterson, R. J., Reitzel, D. B., Kirby, E., & Cooper, M. C. 2007, *ApJ*, 668, 245
- Gilbert, K. M., Guhathakurta, P., Kalirai, J. S., Rich, R. M., Majewski, S. R., Ostheimer, J. C., Reitzel, D. B., Cenarro, A. J., Cooper, M. C., Luine, C., & Patterson, R. J. 2006, *ApJ*, 652, 1188
- Gilbert, K. M., Guhathakurta, P., Kollipara, P., Beaton, R. L., Geha, M. C., Kalirai, J. S., Kirby, E. N., Majewski, S. R., & Patterson, R. 2009, submitted to *ApJ*
- Grillmair, C. J. 2006, *ApJ*, 645, L37
- Grillmair, C. J., & Dionatos, O. 2006, *ApJ*, 643, L17
- Guhathakurta, P., Ostheimer, J. C., Gilbert, K. M., Rich, R. M., Majewski, S. R., Kalirai, J. S., Reitzel, D. B., & Patterson, R. J. 2005, *ArXiv Astrophysics e-prints (astro-ph/0502366)*
- Guhathakurta, P., Rich, R. M., Reitzel, D. B., Cooper, M. C., Gilbert, K. M., Majewski, S. R., Ostheimer, J. C., Geha, M. C., Johnston, K. V., & Patterson, R. J. 2006, *AJ*, 131, 2497
- Helmi, A., & de Zeeuw, P. T. 2000, *MNRAS*, 319, 657
- Helmi, A., & White, S. D. M. 1999, *MNRAS*, 307, 495
- Holland, S. 1998, *AJ*, 115, 1916
- Ibata, R., Chapman, S., Ferguson, A. M. N., Lewis, G., Irwin, M., & Tanvir, N. 2005, *ApJ*, 634, 287
- Ibata, R., Irwin, M., Lewis, G., Ferguson, A. M. N., & Tanvir, N. 2001, *Nature*, 412, 49
- Ibata, R., Martin, N. F., Irwin, M., Chapman, S., Ferguson, A. M. N., Lewis, G. F., & McConnachie, A. W. 2007, *ApJ*, 671, 1591
- Ibata, R. A., Gilmore, G., & Irwin, M. J. 1994, *Nature*, 370, 194
- Irwin, M. J., Ferguson, A. M. N., Ibata, R. A., Lewis, G. F., & Tanvir, N. R. 2005, *ApJ*, 628, L105
- Johnston, K. V. 1998, *ApJ*, 495, 297
- Johnston, K. V., Bullock, J. S., Sharma, S., Font, A., Robertson, B. E., & Leitner, S. N. 2008, *ApJ*, 689, 936
- Johnston, K. V., Hernquist, L., & Bolte, M. 1996, *ApJ*, 465, 278
- Kalirai, J. S., Gilbert, K. M., Guhathakurta, P., Majewski, S. R., Ostheimer, J. C., Rich, R. M., Cooper, M. C., Reitzel, D. B., & Patterson, R. J. 2006a, *ApJ*, 648, 389
- Kalirai, J. S., Guhathakurta, P., Gilbert, K. M., Reitzel, D. B., Majewski, S. R., Rich, R. M., & Cooper, M. C. 2006b, *ApJ*, 641, 268
- Koch, A., Rich, R. M., Reitzel, D. B., Martin, N. F., Ibata, R. A., Chapman, S. C., Majewski, S. R., Mori, M., Loh, Y.-S., Ostheimer, J. C., & Tanaka, M. 2008, *ApJ*, 689, 958
- Lacey, C., & Cole, S. 1993, *MNRAS*, 262, 627
- Larson, R. B. 1974, *MNRAS*, 169, 229
- Majewski, S. R., Frinchaboy, P. M., Kunkel, W. E., Link, R., Muñoz, R. R., Ostheimer, J. C., Palma, C., Patterson, R. J., & Geisler, D. 2005, *AJ*, 130, 2677
- Majewski, S. R., Ostheimer, J. C., Kunkel, W. E., & Patterson, R. J. 2000, *AJ*, 120, 2550
- Majewski, S. R., Skrutskie, M. F., Weinberg, M. D., & Ostheimer, J. C. 2003, *ApJ*, 599, 1082
- Mateo, M. L. 1998, *ARA&A*, 36, 435
- Newberg, H. J., Yanny, B., Grebel, E. K., Hennessy, G., Ivezić, Ž., Martínez-Delgado, D., Odenkirchen, M., Rix, H.-W., Brinkmann, J., Lamb, D. Q., Schneider, D. P., & York, D. G. 2003, *ApJ*, 596, L191
- Ostheimer, J. C. 2003, PhD thesis, University of Virginia
- Pritchett, C. J., & van den Bergh, S. 1994, *AJ*, 107, 1730
- Richardson, J. C., Ferguson, A. M. N., Johnson, R. A., Irwin, M. J., Tanvir, N. R., Faria, D. C., Ibata, R. A., Johnston, K. V., Lewis, G. F., McConnachie, A. W., & Chapman, S. C. 2008, *AJ*, 135, 1998
- Robertson, B., Bullock, J. S., Font, A. S., Johnston, K. V., & Hernquist, L. 2005, *ApJ*, 632, 872
- Robin, A. C., Reylé, C., Derrière, S., & Picaud, S. 2003, *A&A*, 409, 523
- Rocha-Pinto, H. J., Majewski, S. R., Skrutskie, M. F., & Crane, J. D. 2003, *ApJ*, 594, L115
- Rutledge, G. A., Hesser, J. E., & Stetson, P. B. 1997a, *PASP*, 109, 907
- Rutledge, G. A., Hesser, J. E., Stetson, P. B., Mateo, M., Simard, L., Bolte, M., Friel, E. D., & Copin, Y. 1997b, *PASP*, 109, 883
- Simon, J. D., & Geha, M. 2007, *ApJ*, 670, 313
- Sohn, S. T., Majewski, S. R., Muñoz, R. R., Kunkel, W. E., Johnston, K. V., Ostheimer, J. C., Guhathakurta, P., Patterson, R. J., Siegel, M. H., & Cooper, M. C. 2007, *ApJ*, 663, 960
- Somerville, R. S., & Kolatt, T. S. 1999, *MNRAS*, 305, 1
- Stanek, K. Z., & Garnavich, P. M. 1998, *ApJ*, 503, L131
- VandenBerg, D. A., Bergbusch, P. A., & Dowler, P. D. 2006, *ApJS*, 162, 375
- Venn, K. A., Irwin, M., Shetrone, M. D., Tout, C. A., Hill, V., & Tolstoy, E. 2004, *AJ*, 128, 1177
- Yanny, B., Newberg, H. J., Grebel, E. K., Kent, S., Odenkirchen, M., Rockosi, C. M., Schlegel, D., Subbarao, M., Brinkmann, J., Fukugita, M., Ivezić, Ž., Lamb, D. Q., Schneider, D. P., & York, D. G. 2003, *ApJ*, 588, 824